X-RAY VARIABILITY CHARACTERISTICS OF THE NARROW LINE SEYFERT 1 MKN 766 I: ENERGY-DEPENDENT TIMING PROPERTIES

A. Markowitz[1,2], T.J. Turner[1,3], I. Papadakis[4], P. Arévalo[5], J.N. Reeves[1], L. Miller[6]

[1] X-ray Astrophysics Laboratory, Code 662, NASA/Goddard Space Flight Center, Greenbelt, MD 20771; agm@milkyway.gsfc.nasa.gov

[2] NASA Post-doc Research Associate

[3] Department of Physics, University of Maryland Baltimore County, 1000 Hilltop Circle, Baltimore, MD 21250

[4] Physics Department, University of Crete, P.O. Box 2208, 71003 Heraklion, Greece

[5] School of Physics and Astronomy, University of Southampton, Southampton S017 1BJ, UK

[6] Department of Physics, University of Oxford, Denys Wilkinson Building, Keble Road, Oxford OX1 3RH UK

ABSTRACT

We present the energy-dependent power spectral density (PSD) and cross-spectral properties of Mkn 766 obtained from a six-revolution *XMM-Newton* observation in 2005. The resulting PSDs, which have highest temporal frequency resolution for an AGN PSD to date, show breaks which increase in temporal frequency as photon energy increases; break frequencies differ by an average of ~0.4 in the log between the softest and hardest bands. The consistency of the 2001 and 2005 observations' variability properties, namely PSD shapes and the linear rms-flux relation, suggests the 2005 observation is simply a low-flux extension of the 2001 observation. The coherence function is measured to be ~0.6–0.9 at temporal frequencies below the PSD break, and is lower for relatively larger energy band separation; coherence also drops significantly towards zero above the PSD break frequency. Temporal frequency-dependent soft-to-hard time lags are detected in this object for the first time: lags increase towards longer time scales and as energy separation increases. Cross-spectral properties are the thus consistent with previous measurements for Mkn 766 (Vaughan & Fabian 2003) and other accreting black hole systems. The results are discussed in the context of several variability models, including those based on inwardly-propagating viscosity variations in the accretion disk.

1. INTRODUCTION

Seyfert active galactic nuclei (AGNs) and stellar-mass black hole X-ray binary systems (XRBs) both exhibit rapid, aperiodic X-ray variability that likely originates in the innermost regions of these compact accreting objects. The dominant X-ray radiation is generally thought to be inverse Comptonization of soft seed photons by a hot corona (e.g., Shapiro et al. 1976, Sunyaev & Titarchuk 1980), though the exact geometry is uncertain and numerous configurations have been invoked (e.g., Zdziarski et al. 2003). The X-ray variability can be characterized by fluctuation power spectral density functions (PSDs) which show the "red-noise" nature of the variability at relatively high temporal frequencies in both AGNs and XRBs. Modeling of the broadband PSDs of XRBs usually utilizes some combination of one, two, or more Lorentzians, which tend to dominate in the so-called low/hard energy spectral state, plus a broadband noise component characterized as $(f) \propto f^{-1}$, which tends to dominates in the high/soft state (e.g., in Cyg X-1; see Axelsson et al. 2005).

Broadband PSDs have also been constructed for AGNs, allowing modeling of the overall PSD shape. Specifically, 'breaks' in the power-law PSD models on time scales of a few days or less have been identified for roughly a dozen AGN (e.g., Uttley, McHardy & Papadakis 2002; Markowitz et al. 2003; Vaughan, Fabian & Nandra 2003b, hereafter VFN03; McHardy et al. 2004, 2005), with power-

law slopes $\lesssim$–2 above the break and ~–1 below it. The similarity in Seyferts' and XRBs' broadband PSD shapes and scaling of PSD break time scale with black hole mass (e.g., Markowitz et al. 2003, McHardy et al. 2004), as well as the presence of a linear relation between flux and absolute rms variability (e.g., Uttley & McHardy 2001, Edelson et al. 2002), support the notion of similar X-ray variability mechanisms being present in both classes of accreting compact objects. That is, Seyferts and XRBs are simply scaled versions of each other in black hole mass and X-ray variability time scale

Further support for this picture comes from the observed energy-dependence of the PSD power-law slope above the PSD break. Previous studies of both XRBs (e.g., Nowak et al. 1999a, Lin et al. 2000) and Seyferts (Nandra & Papadakis 2001, VFN03, McHardy et al. 2004, and Markowitz 2005) have suggested that the slope flattens as photon energy increases. In addition, Leighly (2004) found the structure function of the narrow line Seyfert 1 galaxy 1H 0707–495 to flatten towards higher photon energies on time scales $\lesssim$ 3 ksec. No obvious trends in break frequency with energy were reported.

The observed cross-spectral properties, namely the coherence function (Vaughan & Nowak 1997) and time lags, are also similar between Seyferts and XRBs. The coherence is generally seen to be close to unity over a wide range of temporal frequencies in both AGNs and XRBs, though

usually dropping significantly below unity above the PSD break (e.g., Nowak et al. 1999a, 1999b in XRBs; VFN03, McHardy et al. 2004 and Markowitz 2005 in AGN). Relatively harder X-rays are seen to generally lag those at softer X-ray energies, with the lag between bands increasing with increasing energy separation. However, lags are are also observed to increase with decreasing temporal frequency (e.g., Miyamoto & Kitamoto 1989, Miyamoto et al. 1991, Nowak et al. 1999a in XRBs), with time lags usually $\lesssim$1–10% of the Fourier time scale. In the low-hard state of Cyg X-1, the time lags increase in a step-like fashion (e.g., Nowak 2000), which can be explained if the lag at each step is associated with individual Lorentzian components in the broadband PSD. Obtaining time lags via the cross-spectrum requires extremely high quality data with sufficient sampling and number of points. Results for AGN so far have yielded time lag spectra with many fewer pointer than in XRBs, but also showing the general increase in time lags as temporal frequency decreases (Papadakis, Nandra & Kazanas 2001, VFN03, McHardy et al. 2004, Markowitz 2005, and Arévalo et al. 2006a).

Mkn 766 is a well-studied Narrow-Line Seyfert 1, objects in which large-amplitude rapid X-ray variability is commonly observed. Timing properties of Mkn 766 have been studied previously by Vaughan & Fabian (2003; hereafter VF03), who measured the broadband PSD, finding a break from steep PSD power-law slope of $\lesssim$–2.5 to $\sim$–1 near 5e-4 Hz. VF03 also found the slope above the break to flatten from $\sim$–2.7 at soft X-rays to $\sim$–2.2 at hard X-rays; however, they saw no obvious trends in break frequency with energy. VF03 were the first to measure the coherence in Mkn 766. In addition, Vaughan et al. (2003a) observed the linear rms-flux relation in Mkn 766.

In this paper we present the timing properties of Mkn 766 from a 500 ksec long-look with *XMM-Newton* in 2005. The average 0.2–12 keV flux was $\sim$2.5 $\times$ 10^{-11} erg cm^{-2} s^{-1} (e.g., Turner et al. 2006), **Jane/James/Lance: Is this value correct? Which paper should be referenced here, Turner et al. 06 or Miller et al. 06?** just under half that of the 2001 observation, 5.9 $\times$ 10^{-11} erg cm^{-2} s^{-1} (e.g., Pounds et al. 2003). We use the enormous wealth of data available from the 2005 long-look to construct PSDs with the highest frequency resolution see an in AGN PSD so far, yielding tight constraints on PSD break frequency. We confirm the rms-flux relation in the 2005 observation and compare the 2001 and 2005 PSD shapes and rms-flux relations. In one of two companion timing papers, Papadakis et al. (in prep.; hereafter Paper II) revisit the broadband PSD shape, using both data from the 2005 long-look and from *RXTE* monitoring data. They confirm the break near 5$\times$10^{-4} Hz seen by VF03, but use Lorentzians to directly probe similarities with the broadband PSD model shapes of XRBs. In the other paper, Arévalo et al. (in prep.; Paper III) continue the study of the energy-dependent variability properties via Fourier-resolved spectroscopy.

This paper is organized as follows: §2 describes the data reduction. §3 describes the analysis, including measurement of the energy-dependent PSD, variability amplitudes and autocorrelation functions, as well as stationarity tests. §4 describes the cross-spectral properties. The results are discussed in §5 in the context of phenomenological vari-

ability models. Finally, a brief summary is given in §6.

2. OBSERVATIONS AND DATA REDUCTION

Mkn 766 was observed by *XMM-Newton* on 2005 May 23 – 2005 June 3, over revolutions 999–1004. This paper uses data taken with the European Photon Imaging Camera (EPIC), which consists of one pn CCD back-illuminated array sensitive to 0.15–15 keV photons (Strüder et al. 2001), and two MOS CCD front-illuminated arrays sensitive to 0.15–12 keV photons (MOS1 and MOS2, Turner et al. 2001). Data from the pn were taken in Small Window mode; data from both MOSes were taken in Large Window mode. The medium filter was used for all detectors. Light curves were extracted using SAS version 7.0 using standard extraction procedures. Data were selected using event patterns 0–4 for the pn and 0–12 for the MOSes. Hot, flickering or bad pixels were excluded. Source light curves were extracted from circular regions of radius 40''; background light curves were extracted from circles of identical size, centered $\sim$3' away from the source. We checked for pile-up; there was no significant pile-up in the pn and at most a few percent pile-up in the MOSes. The 2–12 keV pn light curve was analyzed for background flares; any data where the pn background rate exceeded 0.2 ct s^{-1} were excluded. Most data excluded occurred at the beginnings or ends of revolutions (most notably, the final 18 ksec of revolution 999 data, the final 17 ksec of revolution 1003, and the final 13 ksec of revolution 1004). This screening also introduced a 10 ksec gap in the revolution 1003 light curve. Because such large gaps tend to reduce the statistical significance of variability parameters derived over the full duration, the light curve was split into two smaller light curves, hereafter designated 1003A and 1003B, for a total of seven virtually uninterrupted light curves. All other gaps introduced by background screening were small (< a few ksec) and in the analyses below, fluxes during gaps were linearly interpolated from adjacent points. Data were extracted over the 0.2–12 keV (total), 0.2–0.7 keV (soft), 0.7–2 keV (medium), and 2–12 keV (hard) bandpasses (also referred to as T, S, M and H bands, respectively, below). Light curves from the three EPIC cameras were summed, using only data taken when all three cameras were in operation simultaneously. Given the wide bands used here, the differences between pn and MOS response shapes have a negligible effect: the average pn and MOS photon energies for each band differed only by small amount. In addition, Mkn 766 is a soft-spectrum source, and the inclusion of the MOS data compared to the pn data alone significantly improved signal/noise in the M and H band. Light curves were binned to 60 s; they are shown in Figure 1. Table 1 lists mean count rates and net exposure times. Fractional variability amplitudes $F_{\rm var}$ were calculated for the S, M and H bands for each light curve, using the formulation of Vaughan et al. (2003a); the results, listed in Table 1, confirm relatively high levels of variability, as expected for a NLSy1.

3. THE ENERGY DEPENDENCE OF THE HIGH-FREQUENCY PSD

The high-quantity (uninterrupted and highly variable) light curves allows us to create a very high quality PSD for Mkn 766; in particular, the temporal frequency resolu-

tion allows very tight constraints in break frequency. §3.1 describes how the PSDs were constructed; §3.2 describes model fits to the PSD shapes.

3.1. *PSD Construction*

The construction of the PSDs is summarized here; for further details on PSD construction, see e.g., Uttley et al. 2002, Markowitz et al. 2003, VFN03, and references therein. Paper II explores the broadband fit using 2–11 keV *XMM-Newton* data and *RXTE* Proportional Counter Array (PCA) monitoring, but since this paper's aim is to explore the PSD behavior across as wide an energy range as possible, we do not consider the *RXTE* data as the PCA bandpass does not go below 2 keV. First, for each of the seven light curves, the mean was subtracted. Periodograms were then calculated for each of the seven light curves separately using a Discrete Fourier Transform (DFT; e.g., Oppenheim & Shafer 1975). All periodogram points from the seven light curves were combined and sorted in temporal frequency. Following Papadakis and Lawrence (1993), they were binned in temporal frequency in groups of 25. The PSD normalization of van der Klis (1997) was used. This process yielded a PSD for each of the T, S, M and H bands, each with a usable temporal frequency range: $3.2 \times 10^{-5} - 8.3 \times 10^{-3}$ Hz. Power at temporal frequencies above $\sim 3 \times 10^{-3}$ Hz were dominated by the white noise power due to Poisson noise; this observed level of power agreed well with predicted values calculated as $P_{Psn} = 2(\mu + B)\mu^{-2}$, where μ and B are the net source rate and background rate, respectively. The PSDs $P(f)$ are plotted in Figures 2a and 3 ($f - P(f)$ space and $f - f \times P(f)$, respectively). Above the break, and below frequencies where the power due to Poisson Noise dominates, the hard band PSD has the highest amplitude, consistent with observations for other AGN and XRBs.

3.2. *PSD Model Fits*

We now discuss model fits to the broadband PSD shape. Narrow features in the PSD (e.g., features which, in the PSDs of XRBs, are usually modeled with narrow Lorentzians and may be identified as quasi-periodic oscillations) are discussed in Paper II. Monte Carlo simulations (e.g., Uttley et al. 2002) are frequently employed in PSD measurement when it is necessary to account for PSD measurement distortion effects and to assign errors to poorly-sampled PSD points. However, for the present PSDs, we expect no aliasing since each of the seven light curves were continuously sampled and large gaps were excluded. The effects of red noise leak from temporal frequencies lower than those sampled here are likely small given the measured PSD shape, and at any rate are assumed not to vary significantly with photon energy. Finally, because each PSD bin contains a sufficient number of unbinned periodogram points (25), PSD errors are normal, removing the need for Monte Carlo simulations to determine PSD errors. We employ least-squares fitting (e.g., Bevington 1969) to determine the PSD amplitude in all fits below. Errors below correspond to $\Delta\chi^2 = 2.71$.

We first fit an unbroken power-law of the form

$$P(f) = A(f/f_0)^{-\beta} + P_{Psn}$$

where the normalization A is the PSD amplitude at the frequency f_0 and β is the power law slope; e.g., positive values of β denote red-noise PSD slopes. P_{Psn} is the constant level of power due to Poisson noise, calculated to be 0.18, 0.34, 0.44 and 0.98 Hz^{-1} for the T, S, M and H bands, respectively. P_{Psn} was added to the model as opposed to being subtracted from the data, to avoid the possibility of obtaining unphysical negative powers. Results for the best-fit model are shown in Table 2; residuals to the fits are shown in Figure 2b. The fits are quite poor; large residuals are apparent and signal the need for a break in the PSD model, e.g., as per VF03.

We next tried fitting broken power-law models. In AGN PSDs, it has not always been clear if the breaks are sharp or instead follow a slow bend.

We fit a sharply-broken power-law model of the form

$$P(f) = \begin{cases} A(f/f_b)^{-\gamma} + P_{Psn}, & f \le f_b \\ A(f/f_b)^{-\beta} + P_{Psn}, & f > f_b \end{cases}$$

Here, γ and β are the power-law slopes below and above the break frequency f_b; A is the PSD amplitude at f_b. We also tested a slowly-broken power-law model,

$$P(f) = Af^{-\gamma}(1 + (f/f_b)^{\beta-\gamma}) + P_{Psn}$$

Here, γ and β are the power-law slopes far below or above, respectively, the rollover frequency f_b. A is the PSD normalization.

Results for the best-fit models with β, γ, f_b and A free are listed in Table 3; residuals are shown in Figures 2c and 2d. The somewhat high values of χ^2 for the T, S and H bands are due to a few outlier points above $10^{-2/5}$ Hz; larger temporal frequency bins would alleviate this problem but decrease the temporal frequency resolution of the PSD. The broken power-law fits are significantly better (at $\ge 99.8\%$ confidence in an F-test) compared to the unbroken power-law model fits. Both sharply- and slowly-broken model shapes yield similar fits. There is no obvious trend in β with photon energy in either case. In the singly-broken fits, γ tends to increase as photon energy decreases. f_b is consistent with increasing as photon energy increases.

We explored if it was significant to keep β and γ thawed in the fits. We repeated the fits, with β and γ frozen at the average value of the S, M and H fits. Results are listed in Table 3. The sum of S, M and H χ^2/dof (degrees of freedom) increased from 518.6/432 to 526.8/434 for the sharply-broken PSDs, and from 521.5/432 to 529.7/438. It is this not significant at greater than the $\sim 1\sigma$ level to thaw β and γ. With β and γ frozen, f_b, which has typical errors of 0.07 in the log, is seen to increase with increasing photon energy (errors do not overlap at the 90% confidence level). Refitting the PSDs with f_b, *beta* and γ frozen yields a total (S+M+H) χ^2/dof of 550.3/441 (sharply-broken) and 561.2/441 (slowly-broken). Compared to the model fits with just β and γ frozen, we find that it is significant at 99.97% (sharply-broken) and >99.99% (slowly-broken) confidence in an F-test to keep f_b thawed in the fits.

The data are not able to significantly distinguish between a sharp break or a slow rollover, and the limited dynamic range of the data precludes testing more complicated PSD model shapes. However, we conclude that for all model fits, regardless of whether the power-law slopes were fixed or frozen in the fits, the data are always consistent with f_b increasing with photon energy. f_b increases

by an average of ~0.3 in the log between and S and M bands, and ~0.1 in the log between and M and H bands. Additionally, considering the lack of obvious trends of β (in both the sharply- and singly-broken fits) or γ (in the slowly-broken fits), the results seem consistent with a scenario wherein the PSD shape for all bands is identical, but the break frequency increases with photon energy.

Finally, fractional variability amplitudes F_{var} for the S, M and H-band light curves, listed in Table 1, show that the medium band is almost always the most variable, a result identical to VF03 and similar to VFN03 for MCG–6-30-15. For light curves associated with red-noise variability processes, F_{var} will be dominated by the longest-term trends; the results here are consistent with Figures 2a and 3 where one can see that at temporal frequencies below $\sim 2 \times 10^{-4}$ Hz, the medium band PSD has the highest amplitude. An F_{var} spectrum for the 2005 observation is presented in Miller et al. (2006) who also demonstrate that the variability in the soft and hard bands is diluted by the presence of less-variable components, namely the Compton reflection spectrum in the hard band and by the **soft excess?** and narrow emission lines in the soft band.

4. STATIONARITY TESTS

Compact accreting black holes display "weakly stationary" behavior in that the mean and variance both show scatter over time (e.g., the linear rms-flux relation seen in Seyferts and XRBs), although both the expectation value of the fractional variability amplitude and the underlying PSD shape is expected to remain constant in time, e.g, over time scales shorter than decades to centuries in AGN.

4.1. PSD consistency

We tested for strong non-stationarity in the form of a change in the shape of the underlying PSD, between the 2001 and 2005 PSDs and between revolutions in the 2005 long-look. For two PSDs observing the same stationary process at two different times, the only difference in PSD values at a given temporal frequency should be consistent with the expected scatter. The scatter in the measured PSD about the intrinsic, underlying PSD follows a χ^2 distribution with two degrees of freedom (e.g., Priestley 1981); Papadakis & Lawrence (1995) thus outlined a method to test for non-stationarity, defining a statistic S to quantify differences between two PSDs. For a stationary process, S will be distributed with a mean of 0 and a variance equal to 1 (see also VFN03).

We calculated PSDs for each revolution from 999 to 1003A using the summed pn+MOS light curves as well as for the *XMM-Newton* observation in 2001 May (revolution 265; see VF03 for details). However, while the pn camera was also operated in Small Window mode in the 2001 observation, the MOS cameras were not in Large Window mode. The 2001 pn data were reduced and analyzed in a manner similar to the 2005 data, yielding T, S, M, and H-band light curves 128.5 ksec in duration. Light curves for the T, S, M and H bandpasses were binned to 60 seconds and truncated to a common duration of 52.2 ksec; PSDs were generated by binning periodogram points by a factor of 25. The S statistic was calculated by summing over temporal frequencies $<10^{-2.6}$ Hz to exclude PSD points that were dominated by power due to Poisson noise. For all

PSD pairs and bandpasses, $|S|$ was found to 0.54 or less. Extending the duration to 75.8 ksec to compare revolutions 265 and 999–1002 and extending the duration to 92.3 ksec to compare revolutions 265 and 1000–2 also yielded similarly small values of $|S|$ ($\lesssim 0.5$) for all bandpasses. To summarize, all values of $|S|$ were less than 1σ for all light curve pairs and bandpasses; we therefore have found no evidence for strong non-stationarity in the PSDs of Mkn 766 at any bandpass from one revolution to the next in the 2005 long-look, or between 2001 and 2005.

4.1.1. The linear RMS-Flux Relation

As another test for the presence of strong non-stationarity between the 2005 and 2001 observations, we measured variability amplitudes in the T-band light curve over short time scales. Specifically, for a stationary process, we expect a linear relation between average rms variability amplitude and flux, or, equivalently, we expected $<F_{var}>$ to be constant in flux. Vaughan et al. (2003a) already established the presence of a linear rms-flux relation in the 2001 observation.

To facilitate comparison to the 2001 pn data, only pn light curves from the 2005 observation were used in this analysis. Light curves from both observations were binned to 60 s. We calculated the flux, F_{var}, and the rms amplitude every 2000 seconds (subtracting off the variance due to Poisson noise). Light curves with only 10 points or less were discarded. Flux, rms amplitude, and F_{var} points for all six revolutions were combined; data were sorted according to flux and binned in groups of 10 to yield averaged fluxes of flux, rms amplitude σ_{rms}, and F_{var}. Results are shown in Figure 4 for both the 2005 long-look (black points) and the 2001 long-look (gray points); the top and bottom panels show the $<\sigma_{rms}>$-flux and $<F_{var}>$-flux relations, respectively. Both observations are consistent with a linear relation between flux and $<\sigma_{rms}>$, as shown in top panel, and are also consistent with $<F_{var}>$ being constant in flux, as shown in the bottom panel. Solid lines show the best-fit relations, calculated assuming equal weighting to all points. Despite the average lower flux in the 2005 observation, both best-fit lines in each panel of Figure 4 have similar slopes and intercepts, suggesting that characteristics of the variability process have not significantly changed since 2001, and the 2005 observation is merely a low-flux extension of the 2001 observation. The positive x-intercepts of the best-fit lines for the $<\sigma_{rms}>$-flux relation suggest the presence of a constant component, qualitatively corroborating the principle-component analysis of Miller et al. (2006). As the x-intercepts for the 2001 and 2005 relations are approximately equal, we infer that the the magnitude of the constant component has not changed significantly between the two observations.

Having established that the variability properties in the 2001 and 2005 observation are identical, we constructed T, S, M and H-band PSDs by combining the 2001 and 2005 pn data. The resulting PSD had slightly higher frequency resolution (~%20 in linear space with the same periodogram binning), but the level of power due to Poisson noise in the M and H bands was about about twice as high compared to the PSDs in §3. We repeated the PSD model fits; we found results generally consistent with those obtained in §3, suggesting that the inclusion of the MOS data did not

significantly bias the fitting results.

5. CROSS-SPECTRAL PROPERTIES

The cross-spectrum is used to quantify interband correlations as a function of temporal frequency; analogous to the fact that the PSD is the Fourier transform of the ACF, the cross-spectrum is the Fourier transform of the CCF. The cross-spectrum is a complex number; coherence and time lags can be derived from the squared magnitude and argument, respectively. Because these quantities in compact accreting objects tend to be temporal-frequency dependent, they cannot be studied using cross-correlation functions alone. Further details of the cross-spectrum and its relevance to XRB and AGN observations can be found in e.g., Vaughan & Nowak (1997), Nowak et al. (1999a), Papadakis, Nandra & Kazanas (2001) and VFN03.

5.1. *The Coherence Function*

The coherence function $\gamma^2(f)$ between two time series measures the fraction of mean-squared variability of one series that can be attributed to other, as a function of temporal frequency. If the two time series are related by a simple, linear transfer function, then they will have unity coherence. The coherence is defined as the magnitude squared of the cross spectrum normalized by the product of each light curve's PSD. Here, we use the discrete versions of the cross-spectrum and coherence functions, given in e.g., §5.2.2 of VFN03.

We correct the coherence function for the influence of Poisson noise by following Eq. 8 of Vaughan & Nowak (1997). We assume that the condition of high coherence and high powers required to use this formulation are valid. Specifically, the intrinsic variability power must be at least a factor of a few times $\sqrt{m} \times P_{\mathrm{Psn}}$, where m is the coherence binning factor (quantified below); this condition is thus valid for temporal frequencies up to roughly $1 - 2 \times 10^{-3}$ Hz.

Coherence was measured for each of the seven light curves for the S, M and H bands separately, then combined, sorted in temporal frequency, and binned in groups of $m=30$ to form the final coherence function for the entire 2005 data set. As shown in Figure 5, the coherence is near unity ($\gtrsim 0.8$–0.9) over temporal frequencies lower than $\sim 6 \times 10^{-4}$ Hz for the S–M and M–H pairs. For S–H, the coherence is much lower, ~ 0.6–0.8, at these temporal frequencies. At temporal frequencies above $\sim 6 \times 10^{-4}$ Hz, the coherence significantly drops sharply, reaching $\gamma^2(f) \lesssim 0.5$ by $\sim 8 \times 10^{-4}$ Hz.

This cutoff at high temporal frequencies can be intrinsic, but could also be due to Poisson noise. Monte Carlo simulations were used as a check on the accuracy of the coherence estimates and to determine if significant deviations from unity could be attributed to the effect of Poisson noise. For each of the seven observed light curves, two light curves were simulated using the same random number seed and assuming identical PSD shapes (the average of the best-fitting singly-broken PSD model for each bandpass pair) to produce two light curves with intrinsic unity coherence. The simulated light curves were rebinned and resampled to match the observed light curve, and rescaled to match the mean observed count rates in the softer and harder bands. Poisson noise was then added

to the data according to the Poisson distribution, i.e., data were randomly deviated using a Gaussian convolved with the square root of the observed mean error squared divided by the sampling time. One hundred sets of simulated data were produced. For each set, the coherence and its uncertainty was calculated as for the real data. At most temporal frequencies below $\sim 10^{-3}$ Hz, the simulated coherence was reasonably close to unity, and the uncertainty in the coherence was in reasonable agreement with the scatter, indicating that the coherence estimation was reasonably accurate. The 90% and 95% lower limits to the coherence were determined. Any measured coherence point lying below these lines thus indicates a drop in coherence that is intrinsic to the source, and not an artifact of the Poisson noise, at 90% or 95% confidence. For most temporal frequencies below $\sim 10^{-3.5}$ Hz, the artificial drop in coherence is small.

The energy-dependence of the high-frequency PSD slope could also contribute to a reduction in measured coherence. The Monte Carlo simulations were repeated, assuming the best-fit sharply-broken power-law model shapes. The effects of Poisson noise were again added. The simulated coherence was typically only 1–2%, 2–5% and 1–3% lower for the S–M, S–H and M–H bands, respectively, compared to simulations assuming identical PSD shapes. The effect of having differing PSD shapes is thus small. The 90% and 95% lower limits to the coherence were determined and are plotted in Figure 5. For most temporal frequencies below $\sim 10^{-3.5}$ Hz, the artificial drop in coherence is again small. However, the observed deviations from unity are generally larger than the artificial drop due to Poisson noise. The decrease in coherence as the energy separation of the bands increases and as temporal frequency increases past $\sim 6 \times 10^{-4}$ Hz is thus likely intrinsic.

Having quantified the decrease in coherence e.g., due to Poisson Noise at each temporal frequency, we added that amount (e.g., as determined by the Monte Carlo simulations) to obtain an estimate of the 'intrinsic' coherence. Fitting the 'intrinsic' coherence functions with exponential decay functions of the form $\gamma^2(f) = C\exp(-f/f_c)$ (f_c is the temporal frequency cutoff and C is a constant) ignoring points above 1.2×10^{-4} Hz, and using least-squares fitting, we find that $\log(f_c)$ for the S–M, S–H and M–H coherence functions are -2.90 ± 0.07, -3.07 ± 0.07 and -2.90 ± 0.07, respectively (errors correspond to $\delta\chi^2 = 2.71$).

5.2. *Temporal Frequency-Dependent Time Lags*

Cross-correlation functions (CCFs) for XRBs and AGN generally show a peak near zero lag but are often asymmetrically skewed towards hard lags (e.g., McHardy et al. 2004), suggesting there is a soft-to-hard time lag of some sort, but it is not a simple delay. We measured the CCFs for each of the seven summed light curves of the 2005 observation as well as for the 2001 pn light curve, using a 300 s binning. Because large gaps such as those between revolutions complicate analysis, we calculated CCFs for each of the seven light curves separately. CCFs were measured using both the Discrete Correlation Function (DCF; Edelson & Krolik 1988) and the Interpolated Correlation Function (ICF; White & Peterson 1994); the bootstrap method of

Peterson et al. (1998) was used to assign errors to lags. All peak lags are consistent with zero, with conservative formal errors of ±300 sec for revolutions 265 and 999–1003A, ±1200 sec for revolution 1003B and ±4500 sec for revolution 1004. The CCFs also exhibit a slight soft-to-hard asymmetric skew. The CCFs thus agree qualitatively with those measured for other AGN and XRBs, and the logical direction is to explore temporal frequency-dependent time lags via the cross-spectrum.

Obtaining sensible measurements of time lags via the cross-spectrum is difficult for observations of AGN, however; it requires the combination of a large quantity of uninterrupted data with a high sampling time resolution and a high variability-to-Poisson noise ratio. VF03 did not measure lags for the 2001 data; we also attempted to derive time lags myself from the 2001 pn data and did not get sensible results.

We used Eqs. 28 and 29 in §5.3.1 of VFN03 to calculate the phase lags $\phi(f)$ at discrete temporal frequencies f from the summed light curves in the 2005 observation, binned to 60 s; time lags were then obtained as $\tau(f) = \phi(f)/2\pi f$. Time lags were calculated for each of the seven light curves separately, then combined, sorted in frequency, and binned in groups of 50. Errors on phase lags were calculated using Eq. 16 of Nowak et al. (1999a); in this formulation we used the coherence function appropriate for each binned point. Sensible lags were obtained for the 4 lowest temporal frequency bins, spanning $5 \times 10^{-4} - 4 \times 10^{-3}$ Hz. The results are shown in Figure 6. Errors are large, primarily because coherence in this temporal frequency range is not optimally close to unity. Using Eqn. 16 in Nowak et al. (1999a), we estimated the effective sensitivity limit on time lag detections due to Poisson noise, using the PSD shape and normalization from best-fit M-band singly-broken PSD model shape in §3. Limits are shown as dotted lines in Figure 6.

Monte Carlo simulations were performed to verify that the time lags were not an artifact of Poisson noise nor of the differing PSD slopes between two bands. The same Monte Carlo simulations run for the coherence function in the previous subsection were used; e.g., light curves were simulated with zero intrinsic time lag between them. Time lags were calculated and binned in a manner identical to the real data. For all simulations, the simulated time lags were close to zero (deviations of the average time lag from zero were <32 s for the lowest temporal frequency bin and <13 s for the next three bins). The average error was also close to the standard deviation of the estimates. We can conclude that the observed time lags are not an artifact of Poisson noise or PSD shape differences, and are henceforth assumed intrinsic to the source.

The time lag spectrum displays the general qualities seen in many previous time lag spectra: a general increase towards lower temporal frequencies and as the energy separation of the bands increases. Fitting a relation of the form $\tau(f) = Cf^a$ yields values for the power-law slope a of -0.46 ± 0.18, -0.93 ± 0.17, and -1.26 ± 0.62 for S–M, S–H and M–H, respectively. Alternatively, assuming that the time lags are proportional to $\tau(f) = Cf^{-1}$ for simplicity allows us to calculate fractional time lags, i.e., the lags' fraction of the temporal frequency. We find that $C = 0.013 \pm 0.003$, 0.020 ± 0.004, and 0.010 ± 0.006 for S–M, S–

H and M–H, respectively, consistent with closure between the three bands. The physical implications of these time lags and comparisons to other objects will be discussed further in section 5.

6. DISCUSSION

An *XMM-Newton* observation of Mkn 766 spanning six revolutions in 2005 caught the source in a relatively low flux state; with the average 0.2–12 keV flux just under half that for a 128 ksec *XMM-Newton* observation in 2001. The data reduction yielded seven long, virtually uninterrupted light curves of this highly-variable source totalling 455 ksec of exposure. The resulting PSD has the highest temporal frequency resolution for an AGN PSD to date, allowing a breakthrough in constraining the break frequency with photon energy, as discussed in §6.1. In addition, time lags have detected in Mkn 766 for the first time; §6.2 discusses the cross-spectral results and compares them to those of other compact accreting objects. Finally, the results are discussed in the context of phenomological variability models in §6.3.

6.1. Summary of PSD Results

The PSD analysis showed that while breaks are significantly detected at all bands, model fits cannot distinguish between a sharp break or a slow rollover despite the high temporal frequency resolution. In general, there are no obvious trends in the power-law slope below or above the break, suggesting that the data could be consistent with a PSD shape which is the same at all bands. Importantly, however, the high temporal frequency resolution allows us to place tight constraints on the break frequency – typically ~0.07 in the log, and much tighter constraints than VF03 or even VFN03 for the three *XMM-Newton* revolutions of data for MCG-6-30-15. The break frequency tends to increases by only ~0.4 in the log between the S and H bands (a factor of ~10 in average photon energy), suggesting that PSD measurement spanning a wider range of photon energies would be needed to more easily separate energy-dependent break frequencies. It is also possible that this phenomenon may not have been widely reported in XRBs because all XRB PSDs rely on *RXTE*'s PCA, which does not detect <2 keV photons.

Most previous Seyfert PSDs simply did not have the lower temporal frequency resolution to detect significant changes in f_b with photon energy such as those seen here. It is plausible that for a limited dynamic range PSD, the effect of having an underlying PSD whose break frequency increasing with photon energy could lead to apparent measurements of β, the power-law slope above the break, flattening with energy. Alternatively, it could be the case that this phenomenon might exist only in Mkn 766; high-quality, high-resolution PSDs are needed for many other Seyferts to determine whether this is the case.

Finally, we find no evidence for the underlying variability process to have changed since the 2001 observation, despite the lower average flux. The PSD shapes between 2001 and 2005 are consistent and both observations appear to have consistent linear rms-flux relations and constant $<F_{var}>$ values.

6.2. Summary of cross-spectral results and comparison to other objects

The coherence is generally flat at temporal frequencies below $\sim 6 \times 10^{-4}$ Hz, with values typically $\sim 0.8 - 0.9$ for S–M and M–H and $\sim 0.6 - 0.8$ for S–H. The coherence drops towards zero at higher temporal frequencies; Monte Carlo simulations show these deviations from unity to be intrinsic to the source and not the result of Poisson noise or energy-dependent PSD shapes. The decrease in coherence as energy separation increases has been reported previously for Mkn 766 by VF03; we in fact see values of the coherence similar to VF03. This similarity again supports the conclusion of §3.1, that there is no evidence for the underlying variability process to have changed significantly between 2001 and 2005 despite the overall lower average flux in 2005.

In other black hole systems, the coherence at temporal frequencies below the break is generally between 0.8 and 1.0, though coherence between bands similar to the S and H bands used here can be as low as ~ 0.6–0.7 (e.g., VFN03 & McHardy et al. 2004); Mkn 766's coherence functions thus agree with those in other compact objects.

As explained in Vaughan & Nowak (1997), coherence between two energy bands can lost if the transfer function relating the light curves is non-linear, or if there are multiple, uncorrelated transfer functions. If multiple flaring regions exist each contribute to the signal in both bands, then it is possible for coherence to be low, even if individual regions yield perfectly coherent variability. This is because each region independently requires the same linear soft-to-hard transfer function in order to yield unity coherence between the final light curves. The fact that coherence in Mkn 766 and several other compact objects is not exactly unity may support some degree of non-linearity present in the transfer functions relating relatively softer and harder bands, and which increases for larger energy separations.

As explained by e.g., Nowak & Vaughan (1996) and Nowak et al. (1999a), the sharp drop in coherence at temporal frequencies above the PSD break could indicate that the corona is dynamic on such short time scales. Such short time scales could be associated with formation time scales or changes in temperature and/or the physical structure of the corona. The relatively high levels of coherence at low temporal frequencies could indicate that the corona is effectively static on long time scales.

We measure temporal-frequency dependent phase lags in Mkn 766 for the first time; lags increase towards lower temp frequency and as energy separation of bands increases, as seen in other black hole systems. Fractional time lags are about 0.01–0.02 the Fourier time scale. These values are consistent with most values measured so far for other AGN (see e.g., Figure 8 of Arévalo et al. 2006a), with fractional time lags usually measured to be $\lesssim 0.2$, though Ark 564's time lag spectrum (Arévalo et al. 2006a) seems to be an exception.

Assuming a PSD break frequency of $10^{-3.4}$ Hz, the Mkn 766 lag spectrum is probing temporal frequencies 0.13–1.00 times the break frequency. We can compare Mkn 766's fractional lags to those measured for Cyg X-1 within $\pm$ a decade of temporal frequency of the PSD breaks. In the low/hard and high/soft state of Cyg X-1, fractional time lags tend towards 0.03–0.1 (e.g., Nowak et al. 1999a), while in the intermediate state, fractional time lags are higher, $\sim$0.1–0.2 (e.g., Pottschmidt et al. 2000). On the basis of these fractional lag values, Mkn 766 is likely not a supermassive analog of Cyg X-1 in the intermediate-state, though we cannot determine on the basis of lags alone if analogy with the low/hard or high/soft state is appropriate. Furthermore, the time lag spectrum is not of high enough quality to distinguish between an intrinsic lag spectrum which is step-like, as in the intermediate state of Cyg X-1, or adheres to a form more resembling a power-law.

6.3. Phenomenological Variability Models

Many models have been invoked to explain the red noise variability properties of Seyferts and XRBs, including shot-noise models (e.g., Merloni & Fabian 2001), rotating hot-spots on the surface of the accretion disk (Bao & Abramowicz 1996), self-organized criticality ("pulse avalanche" models; Mineshige, Ouchi & Nishimori 1994), magnetohydrodynamical instabilities in the disk (Hawley & Krolik 2001), and inwardly-propagating fluctuations in the local accretion rate (Lyubarskii 1997). As noted by Uttley, McHardy & Vaughan (2005), shot-noise models have difficulty reproducing the linear rms-flux relation, and as noted by Vaughan & Nowak (1997) and §5.2, shot-noise models lead to low observed coherence unless each separate emitting region independently has the same linear transfer function between energy bands.

Körding & Falcke (2004) note that a pivoting power-law model seems qualitatively capable of reproducing many of the observed variability characteristics in XRBs (and by extension, Seyferts). This model yields high coherence over a broad range of time scales, ACF peaks which get narrower as energy increases, and phase lags which exhibit a dependency on temporal frequency in a manner similar to those observed.

Thermal Comptonization of soft seed photons by a hot corona is a likely explanation for the X-ray emission. It is supported by X-ray energy spectra, and the soft-to-hard time lags could be attributed to the time scale for seed photons to diffuse through the corona and undergo multiple up-scatterings. However, the simplest Comptonization models do not predict time lags that depend on temporal frequency, as observed. In addition, these models predict that relatively harder energy bands, having undergone more scatterings, will have rapid variability washed out, e.g., variability amplitudes at time scales shorter than the PSD break time scale should decrease with increasing energy, contrary to observations. However, the energy dependence of the PSD could be obtained with a corona whose temperature increased towards smaller radii (Kazanas, Hua & Titarchuk 1997).

A model in which inwardly-propagating variations in the local mass accretion rate $\dot{m}$ are responsible for the observed X-ray variability seems to be able to explain many of the observational results in Seyferts and XRBs (Lyubarskii 1997, Churazov, Gilfanov & Revnivtsev 2001, Kotov et al. 2001, Arévalo & Uttley 2006; see also VFN03 and McHardy et al. 2004). In this model, variations at a given radius are associated with the local viscous time scale, so relatively smaller radii are associated with relatively more rapid variations. Perturbations in $\dot{m}$ propa-

gate inward, until they reach, and modify the emission of, the central X-ray emitting region. The resulting PSD has a $1/f$ form across a broad range of temporal frequencies, the net sum of variations from a wide range of radii. However, if the X-ray emitting region is extended, it essentially acts like a low-pass filter on these $1/f$ variations: with relatively higher-frequency variations imprinted on the light curve originating only from the smallest radii, this produces a cutoff in the high-frequency PSD, as is commonly observed. Kotov et al. (2001) suggested that the spectrum can be a function of radius, with relatively harder emission emanating from smaller radii, and therefore associated with more rapid variability. This class of models thus predicts several additional properties which are observed in Seyferts and XRBs, namely the presence of the linear rms-flux relation, the dependence of coherence and time lags on temporal frequency and on the energy separation of the bands, CCF lags, and short-term variability amplitudes increasing with photon energy.

Arévalo & Uttley (2006) show that if the emissivity indices differ for each band (e.g., harder X-ray emission is more centrally concentrated, as per Kotov et al. 2001), and if the PSD break is at least partly due to filtering produced by having an extended X-ray emission region, then the PSDs will have break frequencies which increase with increasing photon energy. We note that the PSDs plotted in Figure 3 for Mkn 766 bear a striking qualitative resemblance to the simulated PSDs in Figure 2 of Arévalo & Uttley (2006). The bending in the Mkn 766 PSDs is slow, and rollover frequencies are relatively close together, so it is not straightforward to relate break frequencies to emissivity index. However, we note that the 'soft' and 'hard' PSDs in Figure 2 of Arévalo & Uttley (2006), simulated assuming emissivity indices which differ by 2, yield break frequencies which are separated by about a decade. In Mkn 766, the S- and H-band break frequencies are not as separated, suggesting that, in the context of this model, the emissivity indices for the S- and H- bands differ by less than 2. **Patricia - you mentioned in your 23 June email that Phil has an XSPEC routine to fit PSDs and lag spectra by varying emissivity indices – do you think it's needed here? Is this something you can do easily? Also, is this next statement accurate?** Similarly, the relatively small fractional time lags observed in Mkn 766 (0.01–0.02 for the S–H bands) could also be an indication that the difference in emissivity indices for the bandpasses used here is relatively small. **Patricia - in Ark 564, with fractional time lags being so high, is this an indication of large difference in emissivity indices in Ark 564? Are energy-dependent PSD break frequencies observed in Akn 564?**

(I got the impression from VF03 that they though coherence, especially S–H, was a bit lower compared to other objects. I'm not sure I agree. If it is true, though, does that mean that damping could play more of a role in Mkn 766's disk compared to other objects?)

7. CONCLUSIONS

We have analyzed the energy-dependent variability properties of the Narrow Line Seyfert 1 Mkn 766 from a 455 ksec *XMM-Newton* observation. The long, uninterrupted, variable light curves allow us to construct a PSD with the highest temporal frequency resolution for an AGN PSD to date. We find PSD breaks at nearly the same temporal frequencies as VF03, but the break frequencies f_b are seen to increase with photon energy, typically by ~ 0.3 between the S and M bands and by ~ 0.1 between the M and H bands. The data cannot distinguish between a sharply broken or slowly-bending PSD model shape. There is no obvious trend in PSD power-law slopes, and the PSDs are consistent with a universal PSD shape whose break frequency increases with photon energy. Previous Seyfert PSDs lacked the temporal frequency resolution to cleanly detect the energy dependene in f_b; previous reports of high-frequency power-law slope flattening with increasing photon energy can again be understood in the context of a universal PSD shape whose break frequency increases with photon energy.

Variability properties between the 2005 and 2001 observations are consistent with each other, despite a 0.2–12 keV flux in 2005 which is less than half that of the 2001 observation. Comparing the 2001 and 2005 PSDs shows the PSDs to be consistent within the expected scatter. A linear rms-flux relation, or equivalently, constant $<F_{var}>$, was reported for the 2001 observation by Vaughan et al. (2003a). These relations are confirmed for the 2005 observation, and shown to be consistent with the corresponding relations from the 2001 observation.

Cross-spectral properties are qualitatively consistent with those measured for black hole systems previously. The coherence is generally flat at temporal frequencies below $\sim 6 \times 10^{-4}$ Hz, with values typically $\sim 0.8 - 0.9$ for S–M and M–H and $\sim 0.6 - 0.8$ for S–H. The coherence drops towards zero at higher temporal frequencies; Monte Carlo simulations indicate that the drop is intrinsic to the source and not an artifact of Poisson noise or differing PSD shapes.

Temporal frequency-dependent time lags are measured from the cross-spectrum for the first time in Mkn 766. As is the case with time lags in other objects, lags increase as temporal frequency increase and as energy separation of the light curves increases. Fractional time lags are typically $\lesssim 0.2$, consistent with many other Seyferts as well as with the high/soft and low/hard states of Cyg X-1.

The results were discussed in the context of several variability models, including models incorporating inwardly-propagating fluctuations in the local mass accretion rate, e.g., Lyubarskii (1997). Notably, the observed increase in the PSD break frequency with photon energy is qualitatively consistent with the prediction put forth by e.g., Arévalo & Uttley (2006), who model variations in a disk with relatively harder X-ray emission being more centrally concentrated.

REFERENCES

Arévalo, P. et al. 2006a, MNRAS, submitted
Arévalo, P. et al. 2006b, in prep. (Paper III)
Arévalo, P. & Uttley, P. 2006, MNRAS, 367, 801
Axelsson, M., Borgonovo, L. & Larsson, S. 2005, A&A, 438, 999
Bao, G. & Abramowicz, M. 1996, ApJ, 465, 646
Bevington, P. R. 1969, Data Reduction and Error Analysis for the Physical Sciences (New York: McGraw-Hill)
Churazov, E., Gilfanov, M. & Revnivtsev, M. 2001, A&A, 321, 759
Edelson, R. & Krolik, J. 1988, ApJ, 333, 646
Edelson, R. et al. 2002, ApJ, 568, 610
Hawley, J.F. & Krolik, J.H. 2001, ApJ, 548, 348
Kazanas, D., Hua, X.-M. & Titarchuk, L. 1997, ApJ, 480, 280
Körding, E. & Falcke, H. 2004, A&A, 414, 795
Kotov, O., Churazov, E. & Gilfanov, M. 2001, MNRAS, 327, 799
Leighly, K.M. 2004, Prog. Theor. Phys. Suppl., 155, 223
Lin, D., Smith, I.A., Böttcher, M., Liang, E.P. 2000, ApJ, 531, 963
Lyubarskii, Y.E. 1997, MNRAS, 292, 679
Markowitz, A. et al. 2003, ApJ, 593, 96
Markowitz, A. 2005, ApJ, 635, 180
McHardy, I.M., Papadakis, I., Uttley, P., Page, M.J. & Mason, K.O. 2004, MNRAS, 348, 783
McHardy, I.M., Gunn, K.F, Uttley, P. & Goad, M.R. 2005, MNRAS, 359, 1469
Merloni, A. & Fabian, A.C. 2001, MNRAS, 328, 958
Miller, L. et al. 2006, in prep.
Mineshige, S., Ouchi, N.B. & Nishimori, H. 1994, PASJ, 46, 97
Miyamoto, S., Kimura, K., Kitamoto, S., Dotani, T. & Ebisawa, K. 1991, ApJ, 383, 784
Miyamoto, S. & Kitamoto, S. 1989, Nature, 342, 773
Nandra, K. & Papadakis, I. 2001, ApJ, 554, 710
Nowak, M. 2000, MNRAS, 318, 361
Nowak, M. & Vaughan, B. 1996, MNRAS, 280, 227
Nowak, M., Vaughan, B., Wilms, J., Dove, J., & Begelman, M. 1999a, ApJ, 510, 874

Nowak, M., Wilms, J., & Dove, J. 1999b, ApJ, 517, 355
Oppenheim, A. & Shafer, R. 1975, "Digital Signal Processing," (Prentice-Hall Publishing)
Papadakis, I. et al. 2006, in prep. (Paper II)
Papadakis, I., Kazanas, D. & Akylas, A. 2005, ApJ, 631, 727
Papadakis, I. & Lawrence, A. 1993, MNRAS, 261, 612
Papadakis, I. & Lawrence, A. 1995, MNRAS, 272, 161
Papadakis, I., Nandra, K. & Kazanas, D. 2001, ApJ, 554, L133
Peterson, B.M. et al. 1998, PASP, 110, 660
Pottschmidt, K. et al. 2000, A&A, 357, L17
Pounds, K.A., reeves, J.N., Page, K.L., Wynn, G.A. & O'Brien, P.T. 2003, MNRAS, 342, 1147
Priestley, M. 1981, "Spectral Analysis and Time Series," (London: Academic Press Ltd.)
Shapiro, S., Lightman, A. & Eardley, D. 1976, ApJ, 204, 187
Strüder, L. et al. 2001, A&A, 365, L18
Sunyaev, R. & Titarchuk, L. 1980, A&A, 86, 121
Timmer, J. & König, M. 1995, A&A 300, 707
Turner, M.J.L. et al. 2001, A&A, 365, L27
Turner, T.J. et al. 2006, in prep.
Uttley, P. & McHardy, I.M. 2001, MNRAS, 323, L26
Uttley, P., McHardy, I.M. & Papadakis, I.E. 2002, MNRAS, 332, 231
Uttley, P., McHardy, I.M. & Vaughan, S. 2005, MNRAS 359, 345
van der Klis, M. 1997, in Statistical Challenges in Astronomy II, ed. G.J. Babu & E.D. Feigelson (New York: Springer), 321
Vaughan, B. & Nowak, M. 1997, ApJ, 474, L43
Vaughan, S., Edelson, R., Warwick, R. & Uttley, P. 2003a, MNRAS, 345, 1271
Vaughan, S. & Fabian, A. 2003, MNRAS, 341, 496
Vaughan, S., Fabian, A. & Nandra, K. 2003b, MNRAS, 339, 1237 (VFN03)
White, R. & Peterson, B.M. 1994, PASP, 106, 978
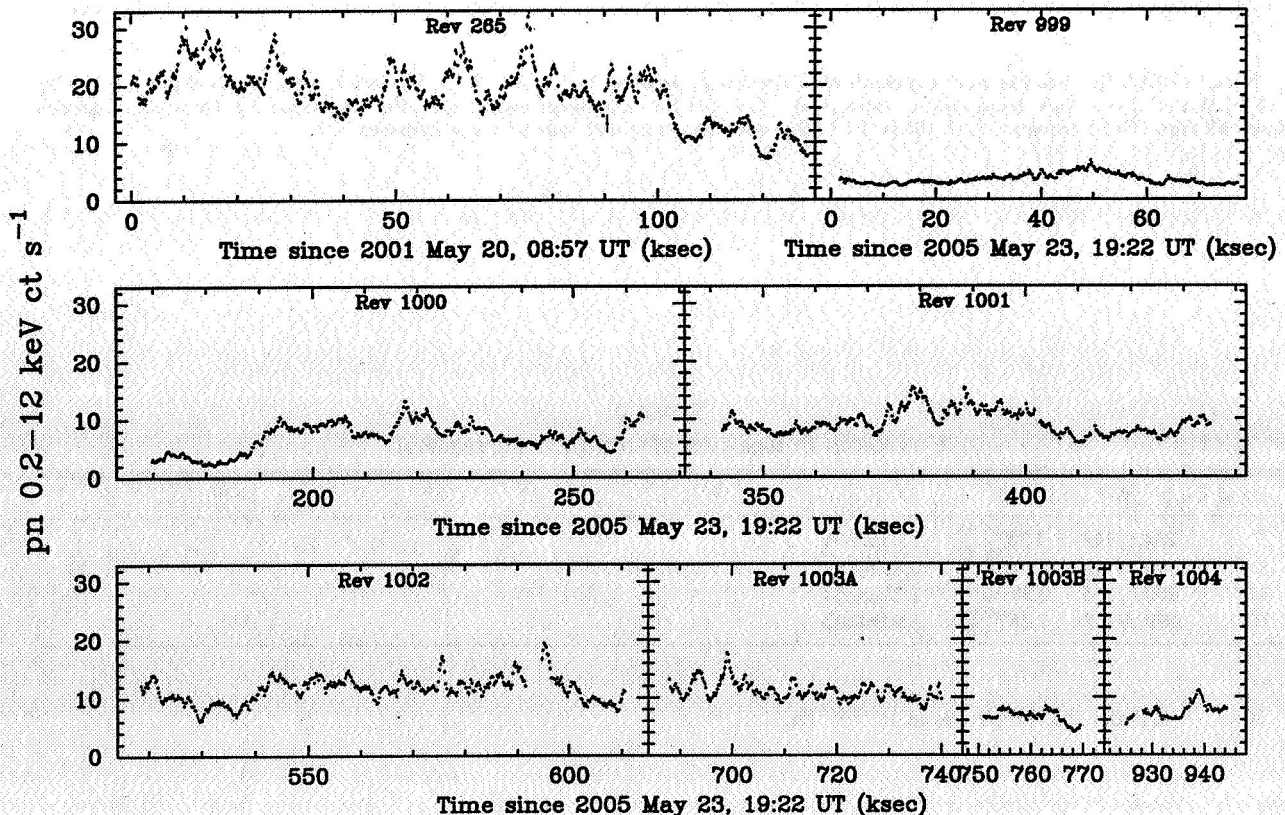Zdziarski, A., Lubinski, P., Gilfanov, M. & Revnivtsev, M. 2003, MNRAS, 342, 355

FIG. 1.— 0.2–12 keV EPIC light curves, summed over the pn and MOS cameras, binned to 60 s, for the 2005 observations. All panels have the same scale.

TABLE 1

SOURCE AND DERIVED VARIABILITY PARAMETERS

Rev.	Exposure (ksec)	Band	Mean ct s^{-1}	Bkgd ct s^{-1}	$F_{\rm var}$ (%)
999–1004	455.0	T	13.44	0.06	40.52 ± 0.04
		S	6.58	0.03	37.56 ± 0.06
		M	4.89	0.01	44.15 ± 0.07
		H	2.22	0.01	32.42 ± 0.10
999	75.8	T	5.65	0.04	24.90 ± 0.15
		S	3.16	0.02	18.91 ± 0.20
		M	1.76	0.01	23.54 ± 0.25
		H	1.30	0.01	22.38 ± 0.29
1000	93.7	T	11.31	0.07	34.36 ± 0.09
		S	5.59	0.03	30.01 ± 0.13
		M	4.12	0.01	38.37 ± 0.15
		H	1.96	0.02	27.65 ± 0.22
1001	93.0	T	15.06	0.06	21.19 ± 0.08
		S	7.35	0.03	22.28 ± 0.12
		M	5.50	0.01	21.71 ± 0.14
		H	2.35	0.01	17.47 ± 0.21
1002	92.3	T	18.65	0.06	18.13 ± 0.07
		S	9.00	0.03	18.59 ± 0.11
		M	6.85	0.01	19.01 ± 0.12
		H	2.91	0.01	17.66 ± 0.19
1003A	52.2	T	18.04	0.06	13.67 ± 0.10
		S	8.46	0.03	13.82 ± 0.15
		M	6.86	0.01	14.28 ± 0.17
		H	2.81	0.01	13.38 ± 0.27
1003B	18.6	T	10.77	0.05	16.60 ± 0.22
		S	5.33	0.03	14.28 ± 0.32
		M	3.83	0.01	18.45 ± 0.37
		H	1.84	0.01	15.45 ± 0.52
1004	19.5	T	12.13	0.06	17.82 ± 0.21
		S	5.86	0.03	12.87 ± 0.31
		M	4.45	0.01	22.29 ± 0.35
		H	2.04	0.02	20.28 ± 0.51

Note. — Col. (2) lists the next exposure after screening, as described in §2. T, S, M, and H refer to the 0.2–12, 0.2–0.74, 0.74–2.0, and 2.0–12 keV bandpasses, respectively. Col. (4) lists the mean count rate after background subtraction, summed from all three EPIC cameras. Col. (5) is the background rate summed over all three cameras.

TABLE 2

UNBROKEN POWER-LAW MODEL FITS TO THE PSD

Band	χ^2/dof	β	A
T	234.8/146	$2.32^{+0.08}_{-0.06}$	1.03 ± 0.04
S	192.7/146	$2.22^{+0.10}_{-0.08}$	0.89 ± 0.03
M	209.9/146	2.20 ± 0.08	1.13 ± 0.03
H	259.2/146	$1.88^{+0.08}_{-0.06}$	1.04 ± 0.03

Note. — A is the PSD amplitude at $10^{-3.50}$ Hz.

| Band	χ^2/dof	γ	$\log(f_b)$	β	A
Sharply-Broken Power-Law Model Fits					
T	170.2/144	1.56±0.16	−3.38±0.06	$2.84^{+0.08}_{-0.12}$	0.98±0.04
S	171.0/144	1.72±0.18	−3.48±0.11	$2.66^{+0.18}_{-0.16}$	1.02±0.03
M	142.6/144	1.40±0.16	−3.35±0.05	2.98±0.20	1.06±0.03
H	205.0/144	1.28±0.14	−3.27±0.06	2.82±0.28	0.87±0.03
T	170.6/146	1.47 (fixed)	−3.41±0.07	2.82 (fixed)	1.06±0.04
S	174.5/146	1.47 (fixed)	−3.53±0.08	2.82 (fixed)	1.20±0.03
M	143.9/146	1.47 (fixed)	−3.36±0.05	2.82 (fixed)	1.05±0.03
H	208.4/146	1.47 (fixed)	−3.23±0.06	2.82 (fixed)	0.75±0.03
Slowly-Broken Power-Law Model Fits					
T	173.5/144	$1.16^{+0.18}_{-0.16}$	−3.49±0.07	$3.00^{+0.12}_{-0.10}$	−2.60±0.04
S	169.1/144	0.80±0.40	−3.92±0.10	2.62±0.10	−0.97±0.03
M	147.2/144	$1.22^{+0.14}_{-0.16}$	−3.29±0.06	3.46±0.26	−2.87±0.03
H	205.2/144	1.14±0.12	−3.17±0.07	$3.42^{+0.40}_{-0.34}$	−2.74±0.03
T	175.5/146	1.12 (fixed)	−3.43±0.06	3.19 (fixed)	−2.49±0.04
S	176.1/146	1.12 (fixed)	−3.55±0.07	3.19 (fixed)	−2.49±0.03
M	148.0/146	1.12 (fixed)	−3.38±0.06	3.19 (fixed)	−2.45±0.03
H	205.6/146	1.12 (fixed)	−3.21±0.07	3.19 (fixed)	−2.65±0.03

Note. —
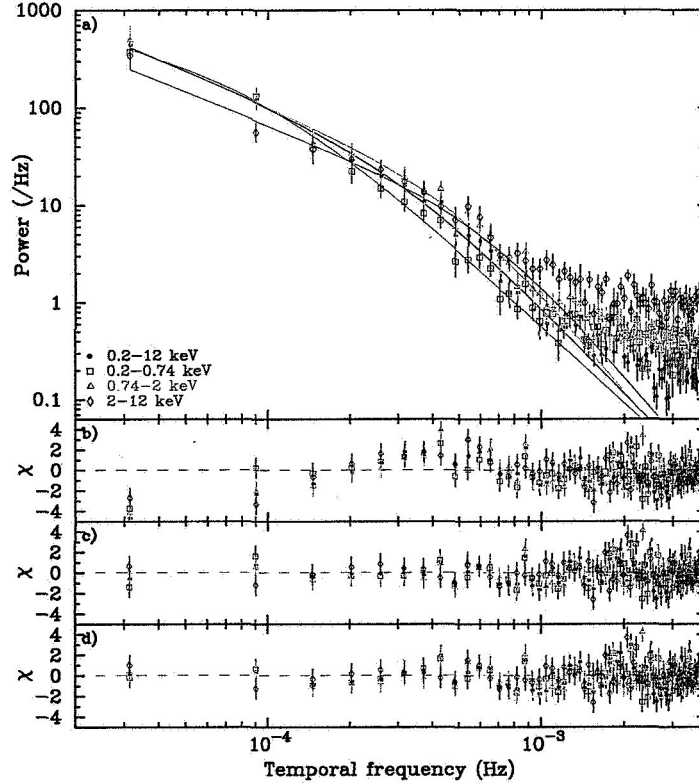
FIG. 2.— a) Power density spectra for the 2005 observation; black, red, green and blue points denote T, S, M and H bands, respectively. See text for details on PSD construction. The solid lines show the best-fit slowly-broken power-law model, though the constant level of power due to Poisson noise has been omitted from the model for clarity. The PSD fits are consistent with break frequency increasing with photon energy. b) Residuals to the best-fit unbroken power-law model. c) Residuals to the best-fit sharly-broken power-law model. d) Residuals to the best-fit slowly-bending power-law model (power due to Poisson noise was included in the models in panels b)–d).
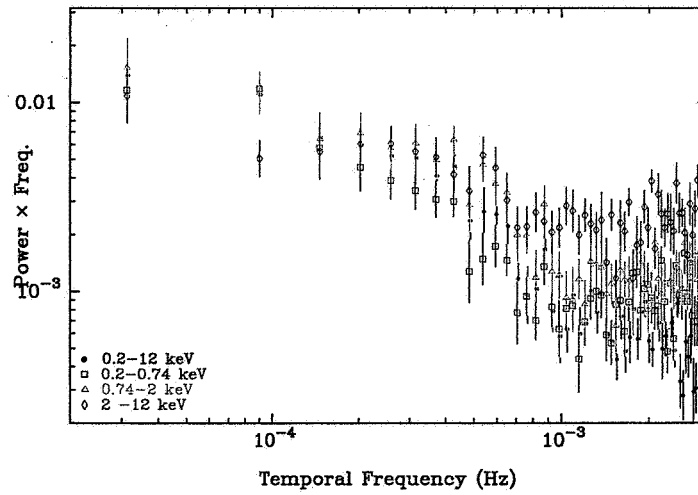
FIG. 3.— PSDs for the 2005 observation, plotted in $f \times P(F)$ space.
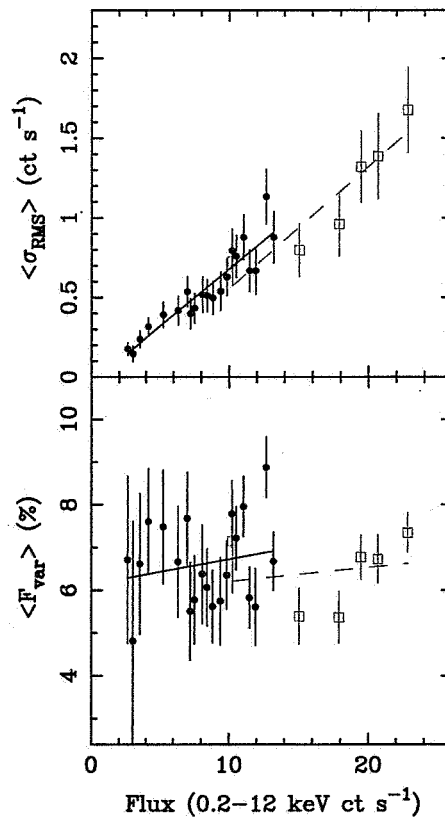

FIG. 4.— The 2005 pn data (black circles) and the 2001 pn data (gray open squares) are both consistent with a linear relation between rms variability amplitude (top) and with constant average fractional variability amplitude $<F_{\mathrm{var}}>$. The black solid and gray dashed lines are the best-fit relations for the 2005 and 2001 data, respectively.
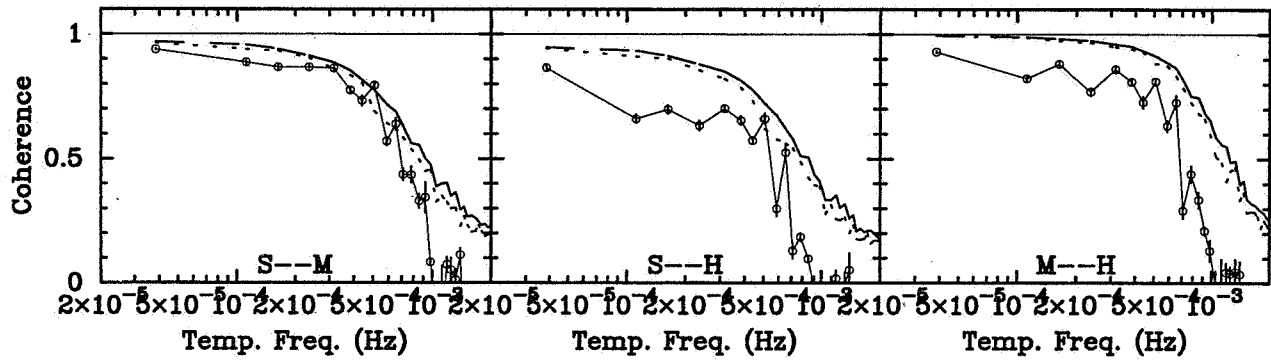
FIG. 5.— Coherence functions for S–M, S–H and M–H light curve pairs. See text for details on calculation of the coherence function. The thin solid line denotes unity coherence. The dashed and dotted lines denote, respectively, the 90% and 95% confidence limits for spurious lack of coherence due to the combination of Poisson noise and the effect of differing PSD shapes.
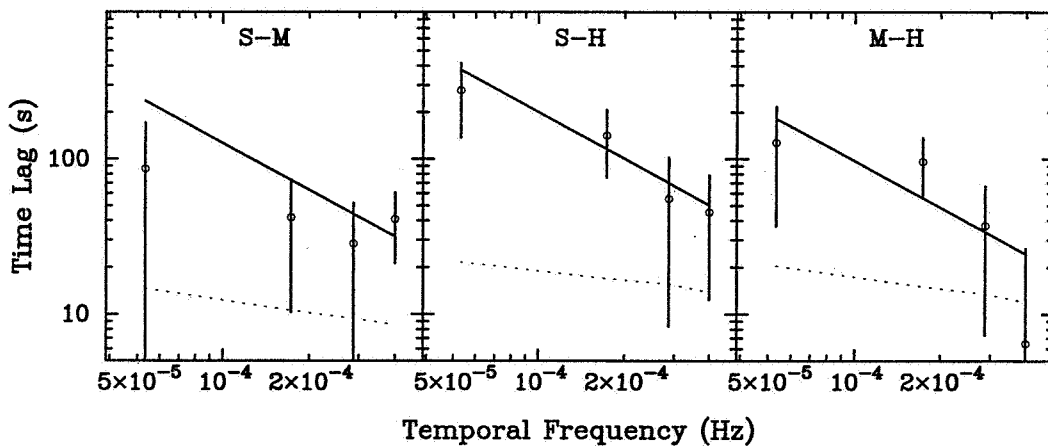

FIG. 6.— Time lag spectra for Mkn 766. Positive lags denote soft band variations leading those in the hard band. The dashed lines denotes the sensitivity limit for time lag detection; see text for details. The solid lines denote the best-fit relations to $\tau(f) = Cf^{-1}$.